Modeling of Thermal Runaway Propagation in a Pouch Cell Stack

Serhat Bilyaz, Kevin C. Marr* and Ofodike A. Ezekoye, Mechanical Engineering, University of Texas at Austin, Austin, TX 78712, USA

Abstract. Characterizing propagation of a thermal runaway hazard in cell arrays and modules is critical to understanding fire hazards in energy storage systems. In this paper, the thermal runaway propagation of a pouch cell array has been examined by developing a 1D finite difference model. The results are compared with experimental data. First, the thermal runaway reactions found in the literature are reviewed. Using the insight of the literature review and premixed flame propagation theory, a global first order Arrhenius type reaction is characterized. While applying the multiple kinetic reactions, an "onset temperature" of the combustion reactions has been determined by performing an induction time analysis on ethylene. The propagation speeds are predicted with a 1D finite difference model by using both multi-reaction kinetics and one step reduced-order kinetics. These results are in a good agreement with experiments for both 10 Ah and 5 Ah cell arrays.

1. Introduction

Lithium-ion batteries are now widely used in various applications such as electronic devices, electric vehicles and large energy storage systems. Despite the increasing usage, their thermal-runaway failure and fire and explosion hazard behavior has not been completely understood. In energy storage applications, multiple cells are used to form compact modules which are designed for capacity and the power requirements of the system. However, the propagation of thermal runaway in such systems is not well characterized.

Fundamentally, thermal runaway is the process in which the energy release rate from exothermic reactions exeeds the rate at which energy is lost from the system through heat transfer. This process is a cell-specific process that can trigger a propagation process between adjacent cells. Thermal runaway propagation may occur by different heat transfer mechanisms in the module depending on the design. Typically, modules that use prismatic and pouch cells contain stacks of cells that are in contact with each other. Therefore, it is critical to understand the

---

* Correspondence should be addressed to: Ofodike A. Ezekoye, E-mail: dezekoye@mail.utexas.edu

heat transfer processes through the cells that affect thermal runaway propagation, called thermal propagation in the remainder of the paper.

Various experimental and numerical studies have been conducted for thermal propagation through cell arrays. Lopez et al. [1] examined the thermal propagation in cylindrical and prismatic cell stacks with various electrical configurations. They concluded that increasing the spacing between cells or inserting insulation material around the triggered cell decreases the thermal propagation risk and the type of electrical connection significantly affects the propagation process. Feng et al. [2, 3] experimentally and computationally studied thermal propagation within large prismatic cell stacks. The initiating cell was failed by a nail penetration failure. The exothermic reaction kinetics were characterised by conducting an Accelerating Rate Calorimetry (ARC) test on a single cell. They suggested that the heat conduction through the battery shell is the dominant propagation mechanism. Their 3D thermal model was able to predict the propagation of cells in agreement with the experimental results. Qi et al. [4] examined the thermal propagation through overcharged large prismatic cells. A 3D thermal model that was coupled to a 1D electrochemical model was used to simulate the failures. The electrochemical model was necessary to estimate the onset of thermal runaway due to overcharging. The Joule heating rate was dominant until thermal runaway began, after which, the heat release rate from cathode reactions exceeded it. The model predictions were in a good agreement with their experimental results. Recently, Gao et al. [5] experimentally investigated cell-to-cell and array-to-array thermal propagation. They tested large prismatic cells and identified three phases of the propagation process. The first phase was slow cell-to-cell propagation. After the propagation started for one array, the propagation speed increased due to an overall temperature increase within the entire battery pack. Said et al. [6] investigated thermal runaway propagation of 18,650 cells in both N_2 and air environment and observed an increase in propagation speed for the air environment.

Since there is relatively thick packaging in large prismatic cells, the propagation time is mainly determined by the conduction phenomena through the non-reactive packaging. However, in pouch cells, the packaging is very thin and the reaction kinetics have more effect on propagation. Therefore, a detailed analysis of various exothermic reactions are required.

Computational studies in the literature either use simple lumped models or computationally expensive 3D models which may include various layers of model complexity in thermal reactions and electrochemistry. Although simple lumped models are fast and have been successfully applied to cylindrical 18,650 cells [1], they are far from accurate representations of the heat transfer physics for both prismatic and pouch cells. In the study with large prismatic cells [3], the kinetic reactions were solved in a lumped sense by using the average temperature of the battery, and applying a uniform heat generation rate to the 3D model. Despite the benefits of the computational cost reduction, the spatial resolution of the kinetics was missing [2–4].

In this paper, thermal propagation in pouch cell arrays has been modeled using a 1D finite difference approach. According to the literature and our previous study, thermal conductivity of the battery in the in-plane direction is about 25

times greater than that in the through-plane direction. Since thermal runaway propagation should be determined in the through-plane direction, heat diffusion should be accurately solved in that direction. A 1D model provides sufficient spatial resolution for heat transfer with less computational expenses compared to 3D models. Thus, more detailed thermal runaway kinetics can, in general, be applied. For this work, first, a literature review is conducted to organize the various possible reactions that are studied in the literature. Using the insight gained from the literature kinetics together with laminar flame propagation theory, a global first-order Arrhenius reaction model is parametrized to simulate our experimental results. Both multi-reaction literature kinetics and global first-order kinetics were tested in a 1D finite difference model to predict thermal propagation in 10 Ah and 5 Ah pouch cell arrays.

2. Organizing Thermal-Runaway Kinetic Data

2.1. *Anode Reactions*

Thermal runaway mechanisms of lithium ion batteries have been summarized in various review articles [7, 8]. At elevated temperatures, there are multiple exothermic reactions in the battery that may trigger a thermal runaway event. In the anode, typically, four reactions are observed which are SEI decomposition (A1), SEI regeneration (A2), Li-electrolyte reaction (A3) and the anode-binder decomposition (A4) [9–12].

If a cell is externally heated, first the SEI layer decomposes at around 90°C and releases heat. Although the amount of heat is not very significant, the decomposition of this protective layer triggers other reactions. The SEI decomposition reaction is modeled by Richard and Dahn [10] as

$$\frac{dx_f}{dt} = -Ax_f^{0.5} \exp\left(-\frac{E}{RT}\right) \tag{1}$$

$$Q_{SEId} = m_{an} h_{SEId} \left(-\frac{dx_f}{dt}\right) \tag{2}$$

In this model x_f is the mole fraction of the metastable part of the SEI and has a value of 0.1 before the decomposition [10].

After the original SEI film decomposes, the intercalated lithium reacts with the electrolyte and deposits on the degenerated SEI film and regenerates a new film. This SEI regeneration (SEI-R) reaction was also studied by Richard and Dahn [10] and the following model was proposed.
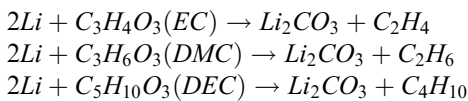
$$\frac{dx_i}{dt} = -A\left(\frac{z_0}{z}\right) \exp\left(-\frac{z}{z_0}\right) \exp\left(-\frac{E}{RT}\right) \tag{3}$$

$$\frac{dz}{dt} = A\left(\frac{z_0}{z}\right) \exp\left(-\frac{z}{z_0}\right) \exp\left(-\frac{E}{RT}\right) \tag{4}$$

$$\dot{Q}_{SEIR} = m_{an} h_{SEIR} \left(-\frac{dx_i}{dt}\right) \tag{5}$$

x_i is the amount of intercalated lithium in the graphite anode and z is the thickness of the new SEI. For a fully charged cell, $x_i = 0.75$ and it is reduced to a value of approximately 0.45 after the reaction in the ARC test [10]. Typically, this reaction represents a peak at around 200°C. There are various views taken about how to address the SEI decomposition and regeneration processes. Feng et al. [8, 13] proposed that the SEI decomposition mechanism should be reconsidered to include the feedback effect of the regenerated SEI. It is possible that these mechanisms have already been included in Richard and Dahn's [10] work and additional modifications are not necessary since they determined the parameters for these reactions from ARC tests, which include all SEI mechanisms. Both SEI-d and SEI-R reactions were modeled and calibrated at once, which should comprise all mechanisms that may occur during SEI-d and SEI-R. As such, in this paper, the kinetic parameters from Richard and Dahn have been used with no modifications.

At elevated temperatures, the secondary SEI (regenerated) also decomposes and the lithium directly reacts with the electrolyte. This reaction (A3) is faster and more energetic than the SEI regeneration (A2) process which consumes the intercalated lithium in the anode and generates hydrocarbons. Depending on the type of electrolytes, the following reactions are proposed [7].

$$2Li + C_3H_4O_3(EC) \rightarrow Li_2CO_3 + C_2H_4$$
$$2Li + C_3H_6O_3(DMC) \rightarrow Li_2CO_3 + C_2H_6$$
$$2Li + C_5H_{10}O_3(DEC) \rightarrow Li_2CO_3 + C_4H_{10}$$

Since the lithium electrolyte reaction (A3) rapidly consumes intercalated lithium, SEI regeneration (A2) cannot continue when lithium is depleted. Thus, these reactions should be coupled since they both use the intercalated lithium in the anode. This phenomena is usually not considered by many researchers. Although this may not be significant in studies which focus on the early stages of thermal runaway [14], the SEI-R reaction (A2) produces abrupt peaks at elevated temperatures with fast heating rates. Kriston [15] coupled these two reactions (A2 and A3) as follows

$$\frac{dx_i}{dt} = -A_{SEIR}\left(\frac{z_0}{z}\right) \exp\left(-\frac{z}{z_0}\right) \exp\left(-\frac{E_{SEIR}}{RT}\right) - A_{LiE} x_i \exp\left(-\frac{E_{LiE}}{RT}\right) \tag{6}$$

The 4th anode reaction (A4) is the decomposition of the binder which is modeled by assuming a first order Arrhenius model as

Table 1
Kinetic Parameters Various Exothermic Reactions at the Charged (with Intercalated Lithium) Graphite Anode

Reaction	Ref	E (J/mol)	A (1/s)	n	x_0	z_0	Δh_r (J/g)	Δh_{bat}^{**} (J/g) **
SEI-d	Richard and Dahn [10]	1.351×10^5	1.667×10^{15}	0.5	0.1	–	613	15
(A1)		1.351×10^5	1.667×10^{15}	0.5	0.16	–	613	23
	Hatchard [14]	1.351×10^5	1.667×10^{15}	1	0.15	–	257	9
	Wang [11]	0.786×10^5	5.14×10^6	–	–	–	496	118
SEI-R	Richard and Dahn [10]	1.061×10^5	3.33×10^{10}	Eqs. 3–5	0.75	0.15	818	72***
(A2)		0.772×10^5	1.667×10^6	Eqs. 3–5	0.75	0.15	1330	25***
	Hatchard [14]	1.351×10^5	2.5×10^{13}	Eqs. 3–5	0.75	0.033	1714	67***
	Wang [11]	0.643×10^5	5.9×10^2	–	–	–	1091	–
	Ren [16]	1.061×10^5	6.36×10^9	5.5	1	–	579	96***
Li + Elec	Wang [11]	–	–	–	–	–	139	33
(A3 or AnE)	Ren [16]	2.001×10^5	5.151×10^{17}	1	1	–	253	60
	Kriston [15]	1.617×10^5	1.78×10^{14}	1	1	–	479	114
Anode-binder	Maleki [12]	1.25×10^5 *	1.61×10^{10} *	1	1	–	837	199
(A4 or AnB)	Wang [11]	–	–	–	–	–	617	147
	Ren [16]	1.955×10^5	4.97×10^{15}	1	1	1	108	26
	Kriston [15]	0.935×10^5	5.62×10^6	1	1	1	208	50

*Calculated from the given data
**Based on in-lab measurements of anode mass (23.8% of the battery mass)
***Evaluated by solving with An–E reaction

$$\frac{dY}{dt} = -A Y exp\left(-\frac{E}{RT}\right) \tag{7}$$

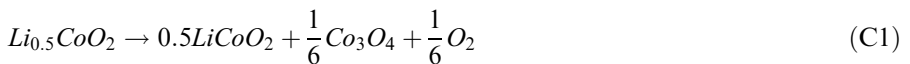$$\dot{Q}_{AnB} = m_{an} h_{AnB}\left(-\frac{dY}{dt}\right) \tag{8}$$

Kinetic parameters of the anode reactions are tabulated in Table 1. Heat of reactions are given per mass of anode material. They are also provided on a per battery mass basis to assess their heating contribution in a real cell and to compare them with the cathode reactions, which will be discussed in the next section. Please note that the anode mass fraction in the pouch cell is taken as 22.8%, which is based on in-lab measurements after tearing down and drying our pouch cells.

2.2. Cathode Reactions and Combustion

At the cathode side, the charged electrode decomposes and releases oxygen. For an LCO cathode, various researchers observed exothermic reactions in ARC and DSC tests. [17–22]. MacNeil and Dahn studied the LCO decomposition by performing ARC and DSC tests and examined various modeling options to characterize them. [17–20] They observed two main peaks at elevated temperatures (180°C to 230°C) and associated the released heat with the oxidation of the electrolyte. In the presence of excess electrolyte, they also observed another exothermic reaction at temperatures around 500°C, but did not characterize it since it did not consistently occur in all tests. Baba et al. [22] mentioned that the heat released at around 190°C is associated with a structural change of the LCO. They performed X-Ray Diffraction testing (XRD) before and after the first peak of their DSC test (one at room temperature and the other at 220°C) and showed that the delithiated LCO changed its monoclinic (R3m) structure to a spinel structure (Fd3m). They concluded that the exothermic reaction at around 190°C is not related with electrolyte oxidation, but phase transformation and oxidation happens after 230°C. Wang et al. [23] discussed the thermodynamics of this phase transformation and oxygen release of Li_xCoO_2 and showed that the layered phase is more unstable then the spinel structure and the transformation is expected for delithiated LCO. They also mentioned that for x < 0.5, this transformation may also release oxygen.

Wang et al. [21] conducted DSC tests to investigate the effect of electrolyte on delithiated LCO decomposition. The rinsed and dried LCO showed an exothermic peak at around 250°C. Since the sample also contained binder and acetylene black (carbon black), it is not clear if this heat release is due to the layered-to-spinel transformation or oxidation. Their sample with electrolyte showed earlier and much sharper peaks than the rinsed and dried sample. Jiang and Dahn [24] explained these temperature shifts as the "reducing power of the solvent". Since the electrolyte is a significant oxygen sink, the oxidation might happen earlier than expected.

The decomposition of fully charged LCO occurs in 3 stages.

$$Li_{0.5}CoO_2 \rightarrow 0.5LiCoO_2 + \frac{1}{6}Co_3O_4 + \frac{1}{6}O_2 \tag{C1}$$

$$Co_3O_4 \rightarrow 3CoO + \frac{1}{2}O_2 \tag{C2}$$

$$CoO \rightarrow Co + \frac{1}{2}O_2 \tag{C3}$$

In the presence of electrolyte, the first two stages occur sequentially within a temperature range of 200°C to 500°C. If there is still excess electrolyte at temperatures greater than 500°C, the third stage is also observed [20].

In order to characterize the oxygen release from the LCO, Yamaki [25] used thermogravimetry and mass spectrometry (TG–MS) to detect the oxygen release at various rates of temperature scanning. They observed oxygen above 240°C. One step global oxygen release rate equations are developed for various delithiation amounts. Furushima et al. [26] used temperature programmed desorption–mass spectrometry (TPD–MS) and observed oxygen generation after 250°C. Recently, Jung et al. [27] used temperature programmed reduction technique to identify the reaction kinetics of all three stages related with the oxygen release.

First and second stages of the LCO decomposition reaction are modeled by using an Avromi–Erofeev type of reaction, which is suitable for solid phase transform reactions. MacNeil and Dahn [19] investigated various reaction types for LCO decomposition and considered a general form as

$$\frac{d\alpha}{dt} = A\alpha^m (1-\alpha)^n (-\ln(1-\alpha))^p \exp\left(-\frac{E}{RT}\right) \tag{9}$$

where α is the conversion rate, which is parametrized using the ARC test data. They found that the best results were obtained using m = 0, n = 1 and p = 2/3. For that model, α starts at a value of 0.03 and reaches a value very close to 1 when the reaction ends.

For the third stage, a first order reaction model is used, which can be written as

$$\frac{d\alpha}{dt} = A(1-\alpha) \exp\left(-\frac{E}{RT}\right) \tag{10}$$

For each cathode reaction, the heat generation can be written as

$$\dot{Q}_{LCO,i} = m_{cat} h_{cat,i} \left(\frac{d\alpha_i}{dt}\right) \tag{11}$$

In addition to the oxygen generated by the charged LCO, there might be oxygen available outside the cell which might burn discharged flammables from the cell and the plastic packaging. Since the experimental data used in this paper is conducted in an inert environment, the combustion is only considered due to the oxygen generated by the LCO decomposition.

Since the cathode includes binder material, a binder decomposition reaction is also expected, which has been identified by many researchers. [15, 16, 28] A first order Arrhenius reaction is used for the binder decomposition in the cathode.

$$\frac{dY_{CatB}}{dt} = -A_{CatB} Y_{CatB} exp\left(-\frac{E_{CatB}}{RT}\right) \tag{12}$$

$$\dot{Q}_{CatB} = m_{cat} h_{CatB} \left(-\frac{dY}{dt}\right) \tag{13}$$

Kinetic parameters for the cathode reactions are tabulated in Table 2. Although the samples with electrolyte are more realistic for a full scale cell, the studies in absence of electrolyte are also provided. Since Yamaki [25] and Jung's [27] studies focus on oxygen generation, they did not provide a heat of reaction. Baba et al. [22] estimated a total heat of reaction of 1400 J/g, but their sample did not contain binder. According to the Wang's study [21], we have considered a total heat of reaction of 1450 J/g. To evaluate Yamaki's and Jung's kinetics, we have distributed this amount to the corresponding stages such that the first two stages have the heat of reactions of MacNeil and Dahn [20] and Kriston et al. [15] and the third stage has the remaining from the total.

2.3. Evaluation of Literature Kinetics

Before implementing the various reactions to the 1D finite difference model, the kinetic models are tested by using a lumped model. If the battery is considered to be a homogeneous medium, heat generated by the individual reactions are distributed to the battery mass according to the following.

$$m_{bat}c_{p,bat}\frac{dT}{dt} = \sum_i \dot{Q}_{rxn,i} \tag{14}$$

The temperature rise of the battery is decomposed to its contribution from individual reactions as

$$\left(\frac{dT}{dt}\right)_{rxn,i} = \frac{\dot{Q}_{rxn,i}}{m_{bat}c_{p,bat}} \tag{15}$$

The cell is considered to be thermally and chemically lumped and heated at a specified rate. This can be considered to be synthetic DSC data. The external heating is controlled such that it is provided unless the total heating rate of the reactions is not sufficient to reach the specified heating rate. Thus, the heating rate of the lumped cell can be written as

$$\frac{dT}{dt} = \begin{cases} \left(\frac{dT}{dt}\right)_{heater}, & \left(\frac{dT}{dt}\right)_{rxns} < \left(\frac{dT}{dt}\right)_{heater} \\ \left(\frac{dT}{dt}\right)_{rxns}, & otherwise \end{cases} \tag{16}$$

The equations can be integrated together by using an explicit RK45 method, starting with an initial condition of 80°C. Then, the contribution of various reactions can be extracted.

The heat release rate of various anode reactions are presented in Fig. 1. It can be seen that the SEI-d (A1) starts around 100°C. Richard and Dahn [9, 10] and Hatchard et al. [14] SEI-d (A1) reactions contribute very little to the heating of the battery. Wang [11] parameters represented very high high heat of reaction compared to the others, which might be specific to their battery since the heat of reaction varies according to the carbon surface area of the anode. Since Kriston

Table 2
Kinetic Parameters of Reactions at the Charged (Delithiated) LCO Cathode

Reaction Stage	Ref	Sample	E (J/mol)	A (1/s)	m	n	p	α_0	Δh_r (J/g)	Δh_{bat}^{**} (J/g)
C1	MacNeil and Dahn [19]	LCO + Elec	1.194×10^5	6.67×10^{10}	0	1	2/3	0.03	257	113
C1	Hatchard [14]	–	1.226×10^5	6.67×10^{11}	1	1	0	0.04	314	138
C1	MacNeil and Dahn [20]	LCO + Elec	1.138×10^5	1.27×10^{10}	0	1	2/3	0.03	470	207
C2	"	LCO + Elec	1.407×10^5	2.33×10^{12}	0	1	2/3	0.03	280	123
PT****	Baba [22]	LCO + Elec	–	–	–	–	–	–	400	176
C1 + C2 + C3	"	LCO + Elec	–	–	–	–	–	–	1000	440
C1 + C2 + C3	Wang [21]	LCO + Elec	–	–	–	–	–	–	1456	641
C1	Wang [29]	LCO	0.889×10^5	1.87×10^6	0	1	0	0	489	215
C1 + C2 + C3	Yamaki [25]	LCO	1.140×10^5	1.18×10^8		1.62	0	0	1450***	638
C1	Jung [27]	LCO	0.919×10^5 *	1.254×10^7 *		1	0	0	470***	207
C2	"	LCO	1.256×10^5 *	1.33×10^8 *		1	0	0	280***	123
C3	"	LCO	1.593×10^5 *	5.71×10^9 *		1	0	0	500***	220
Binder	Ren [16]	NMC	1.779×10^5	2.43×10^{13}	1		–	1	452	199
Binder	Kriston [15]	NMC	1.993×10^5	3.78×10^{12}	1		–	1	212	93

*Calculated from the given data

**Based on in-lab measurements of cathode mass (44% of the battery mass)

***Assumed based on MacNeil and Dahn [20], Baba et al. [22] and Wang et al. [21]

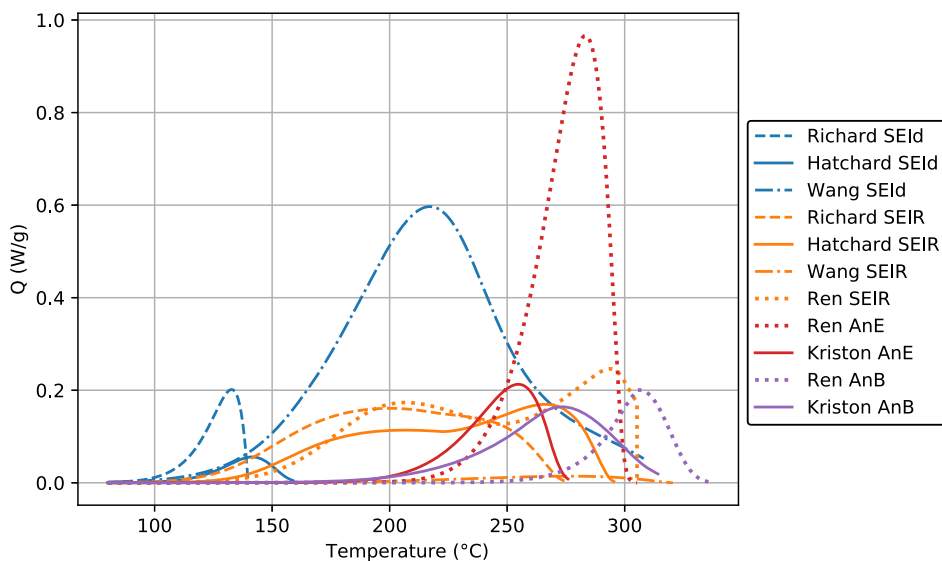****Baba et al. [22] attributed this stage to the phase transformation rather than oxidation

Fig. 1. **Heat release of various anode reactions per battery mass for 10°C/min external heating rate.**

et al. [15] and Ren et al. [16] did not observe a low temperature peak associated with SEI decomposition, we believe that this reaction has a very small effect. Figure 1 also shows that the SEI regeneration (A2) profiles are consistent with each other. This reaction slowly heats the cell over a wide temperature range.

SEI regeneration (SEI-R) heat of reactions may be misleading unless the effect of the anode–electrolyte (An–E) reaction is considered. The An–E reaction quickly consumes the amount of intercalated lithium such that the contribution of the SEI-R reaction will only be around 30% of the given heat of reactions. In order to have a better idea, Δh_{bat} values that are given in Table 1 are evaluated by solving SEI-R (A2) with An–E (A3) reaction and calculating the contribution of the SEI-R reaction alone.

Anode–electrolyte (A3) and anode-binder (A4) reactions are within comparable temperature ranges in both Ren's [16] and Kriston's [15] studies. Ren's AnE reaction (A3) represents higher peak compared to all other reactions.

The heat release rates of cathode reactions are presented in Fig. 2. Since the scales are different, two axes are used. MacNeil and Dahn's [20] and Yamaki's stages have very large heat release rates compared to others. The MacNeil and Dahn's test had the LCO sample with electrolyte, which is a more realistic scenario. The Hatchard [14] and MacNeil and Dahn [19] peaks occur at lower temperatures compared to others. If the total heat of reaction is around 1460 J/g (Baba et al. [22], Wang et al. [21]), MacNeil's two stage [20] (750 J/g) and a cathode-binder reaction [15] ($\sim$ 200 J/g) do not sum to the total value. Therefore, a 3rd stage should also be considered. Since there is a lack of information about the decomposition of these reactions, we will not speculate on what this might be.
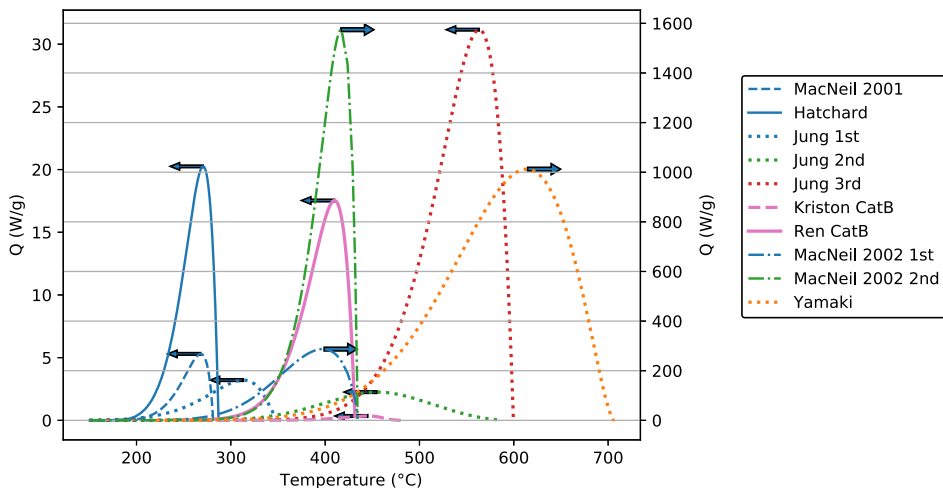
Fig. 2. Heat release of various cathode reactions per battery mass for 10°C/min external heating rate.

Depending on the heater rate, these kinetics may represent different behavior. A thermal propagation problem may be similar to a very fast heating case. For various heater rates, all reactions are solved together. For SEI Reactions we use Richard and Dahn's data [9, 10]. For the AnE, AnB and CatB reactions we use Kriston's data [15]. For the first and second cathode reactions we use MacNeil and Dahn's data [20]. For the third cathode reaction we use Jung's parameters [27] and models.

Total heat generation is plotted with respect to the temperature in Fig. 3. If the heating rate is faster, the heat generation occurs in shorter times and the range of the reactions is shifted to higher temperatures. The heat generation rate is fast and energetic after approximately 300°C. The first peak is associated with the combination of the first and second cathode reactions. The second peak after 600°C is a combination of the third cathode reaction and binder decomposition reaction in the cathode.

3. Parametrization of Reaction Kinetics Using Laminar Premixed Flame Propagation Theory

Up until this point we have only discussed cell reaction kinetics. These cell kinetic effects are critical to propagation processes. To connect the cell-based kinetics to propagation, we use the well known laminar premixed flame theory [30]. A first-order Arrhenius kinetics is parameterized in this section using that theory.

The integrated energy equation for an advection–reaction balance can be written as [30]

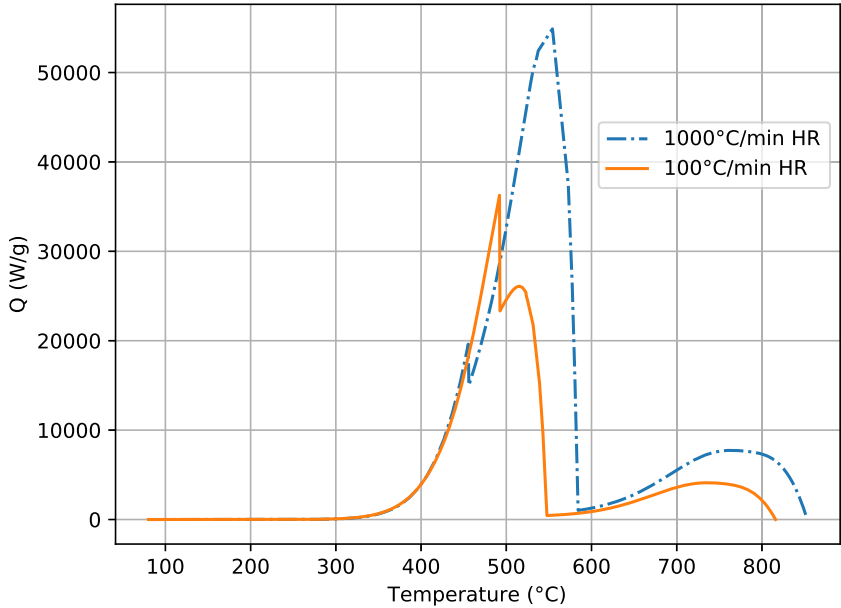$$\rho_u S c_p (T_b - T_u) = \delta \Delta h_R \overline{\dot{\omega}_F'''} \tag{17}$$

Fig. 3. Total heating rate of anode and cathode reactions evaluated at various heating rates.

where S is the propagation speed, Δh_R is the heat of reaction and $\overline{\dot{\omega}_F'''}$ is the average volumetric fuel consumption rate.

This equation relates the propagation speed to the average fuel consumption rate. However, the reaction zone thickness (δ) is an unknown here, but it can be estimated using the integral energy equation for the unburned thermal zone.

$$\delta = \frac{k}{c_p \rho_u S} \left(\frac{T_b - T_{xf}}{T_{xf} - T_u} \right) \tag{18}$$

For a first order Arrhenius type reaction, the average fuel consumption rate can be written as

$$\overline{\dot{\omega}_F'''} = \frac{\rho_u A}{T_b - T_{xf}} \int_{T_{xf}}^{T_b} Y \exp\left(-\frac{E}{RT}\right) dT \tag{19}$$

Since there is no fuel mass diffusion in the cell, the dimensionless fuel concentration varies from 1 to 0 at x_b and x_{xf} respectively. If a linear relation is assumed with respect to the temperature, an integral parameter (I) can be written as

$$I = \int_{T_{xf}}^{T_b} \frac{T - T_b}{T_{xf} - T_b} \exp\left(-\frac{E}{RT}\right) dT \tag{20}$$

Equation 20 can be evaluated numerically for any given activation energy, which leads to an estimation for a frequency factor for the reaction as

$$A = \frac{\overline{\dot{\omega}_F'''}(T_b - T_{xf})}{\rho_u I} \tag{21}$$

Please note that A is the frequency factor of the first order Arrhenius type reaction.

In order to evaluate the frequency factors, the activation energy (E), reaction onset temperature (T_{xf}), heat of reaction (Δh_R) and propagation speed (S) are required. From our literature survey, we expect the first reaction of the reaction cascade is the SEI-R reaction. Therefore, the activation energy and onset temperature of the SEI-R reaction are used: $E = 1.061e5$ J/mol and $T_{xf} = 200$ °C. Similarly, a total heat of reaction of $\Delta h_R = 900$ J/g is expected (~ 250 J/g from anode reactions and ~ 650 J/g from cathode reactions), which leads to a burned temperature of $T_b \cong 700$ °C. From the 10 Ah cell array experiment, an average propagation speed of $S = 0.42$ mm/s is calculated. The reaction zone thickness is estimated as $\delta = 1.73$ mm. Using this information, the estimated average fuel consumption rate and frequency factor are calculated as $\overline{\dot{\omega}_F'''} = 579.69$ kg/m^{3}s and $A = 8.29e6$ s^{-1} respectively.

4. Thermal Runaway Propagation in Cell Array

4.1. *Experimental*

Experimental data used in this study were conducted with polymer 3.7 V 10 Ah and 5 Ah lithium-ion pouch cells. The cells are based on lithium-cobalt-oxide (LCO) cathode and graphite anode. The electrolyte is a mixture of DMC:DEC:EC and LiPF$_6$ salt. 10 Ah cells have a weight of 208.9 g and dimension of 150.38 mm $\times$ 57.775 mm $\times$ 10.409 mm. 5 Ah cells have a weight of 90.26 g and dimension of 67.44 mm $\times$ 62.10 mm $\times$ 8.765 mm. For 5 Ah cell, the specific heat of the cell is calculated by componentwise analysis as 1333 J/kgK and thermal conductivity is predicted as 0.83 ± 0.215 W/mK. [31] In the same study, the thermal conductivity of the calcium silicate insulation block has also been determined as 0.1177 ± 0.0054 W/mK

Cells are sequentially placed to form an array. Calcium silicate insulation blocks with a thickness of 1.27 cm (half inch) are placed at beginning (3 blocks) and end of the array (1 block). At one side, a cylindrical aluminum block with a carthage heater was placed inside the insulation layer, which provides localized heating. The entire stack was clamped using aluminum blocks. Then, the system is placed in a pressure vessel and the first cell was thermally induced with a rate of approximately 100°C/min. The test were performed in a nitrogen environment. Temperature between batteries are measured by using K-type thermocouples. A picture of the experimental set up is given in Fig. 4.
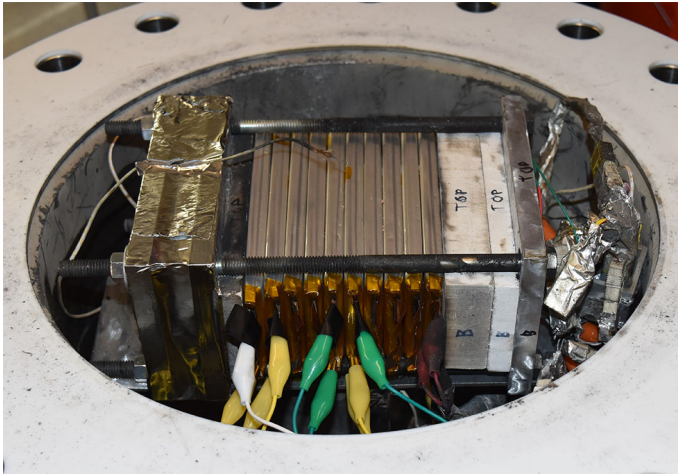
Fig. 4.   Picture of the experimental set-up (10 × 10 Ah test).

Three data sets are used in this study, which are 10 × 10 Ah cells, 5 × 5 Ah cells and 10 × 5 Ah cells. Due to lack of clear data, the last five cells of the 10 × 5 Ah data set are ignored. Temperature measurements of 10 × 10 Ah and 5 × 5 Ah array tests are provided in Fig. 5. 10 Ah cells reached a maximum temperature of 800°C whereas the 5 Ah cells could reach 1000°C. This difference may be due to the energy density of the cells, since 5 Ah cells contain more energy per mass. In the 10 × 10 Ah test, the voltage of cells 5 and 6 in series and cells 9 and 10 in series are also provided. When the temperature began increasing at one side of the cell, a slight voltage drop occurred. The voltage goes to zero after the temperature increased at the other side of the cell. The pouch cell is comprised of multiple layers that are connected in parallel. Voltage measurements may not be meaningful to characterize the type of the failure process since the local potential differences are not measured. The global voltage remains approximately constant until the separator of the last layer is melted.

According to the mass measurement of cells after the experiment, approximately 28% of the mass of 5 Ah cells and 27% of the mass of 10 Ah cells were lost during the thermal runaway, which is approximately the same as the value reported for NCM cells by Feng et al. [2]. Somandepalli et al. [32] performed combustion chamber tests on LCO cells and measured a gas release of 0.325 L/Wh for cells with 100% SOC. According to this, approximately 6 L and 12 L of gas release is expected for our 5 Ah and 10 Ah cells respectively. These amounts correspond to a mass fraction of around 3% of the fresh cell, which is less than the measured 27%. Therefore, the majority of the mass loss is expected to be in uncollected solids such as soot and melted/dripped metals and condensed liquids such as water and unburned electrolyte.
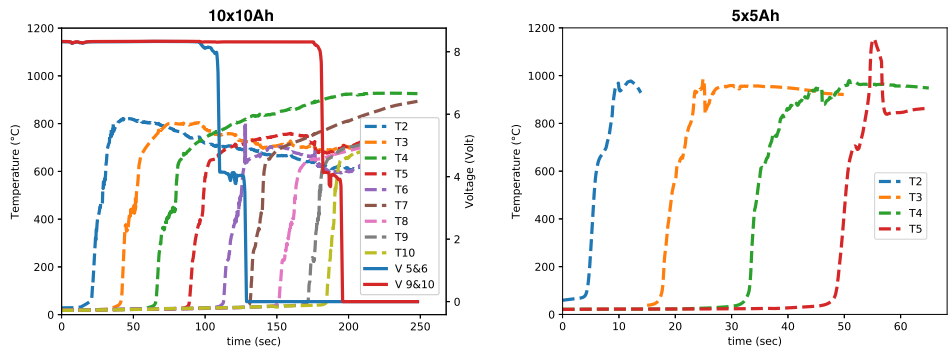
Fig. 5.   Experimental results of 10 × 10 Ah and 5 × 5 Ah tests.

4.2. 1D Finite Difference Model

The heat diffusion equation is solved for the battery stack system by a 1D Finite Difference approximation. A schematic for the system is presented in Fig. 6.

The governing PDE for the heat transfer within the battery can be written as described by Eq. 22

$$\rho c_p \frac{\partial T}{\partial t} = k \frac{\partial^2 T}{\partial x^2} + \frac{hP}{A_c}(T - T_{amb}) + \dot{Q}'''_{rxn} \tag{22}$$

The diffusion term in Eq. 22 is discretized using a second order stencil. The reaction part is handled by operator splitting. In each time step, first the convection–
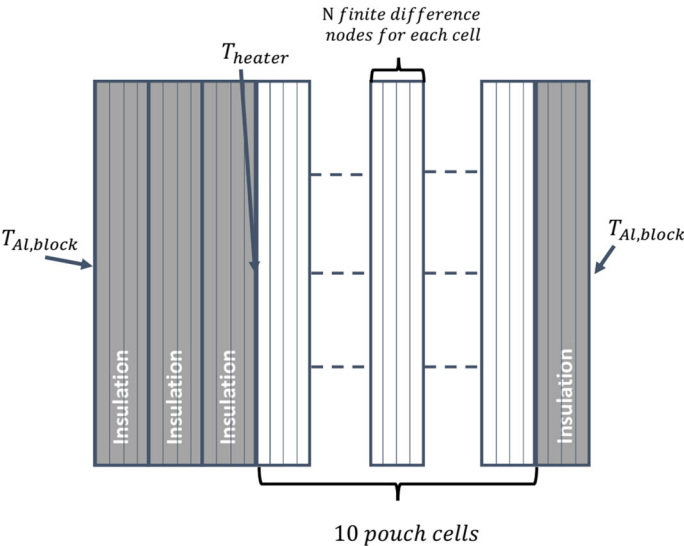
Fig. 6.   Schematic of the cell array.

diffusion part is solved implicitly, then the reaction parts are explicitly solved by using scipy RK45 integrator and added to the solution.

A convective heat transfer is defined for side surfaces. At the outermost side of the insulation, a constant temperature boundary condition is used. Since the system is clamped with aluminum blocks in a natural convection environment, (which corresponds a small Biot number), it is a reasonable assumption. In addition, according to our preliminary calculations, the heat is not expected to reach at the boundaries which supports our selection of the boundary condition.

$$\dot{Q}'''_{rxn} = \sum_i \dot{Q}'''_{rxn,i} \tag{23}$$

Two different approaches are used to model the kinetics. First, a set of kinetics parameters associated with 8 different reactions (4 for anode, 4 for cathode) is selected from literature and applied to the Eq. 23. For the anode, Richard and Dahn's SEI-d (A1) and SEI-R (A2) and Kriston's An–E (A3) and An-B (A4) reaction parameters are selected. For the cathode, MacNeil and Dahn's C1 and C2, Jung's C3 and Kriston's Cat-B reaction parameters are selected.

In applying cathode reactions, the onset temperature has been predicted by examining the ignition time for ethylene. The details of the ignition time calculation are given in the Appendix. We have assumed the oxygen becomes available when $\alpha_1 = 0.031$ (note that the initial condition was 0.03) and the time is stored as τ_{O2}

Since we have an ignition time as a function of temperature $\tau_{ign} = f(T)$ (See "Appendix"), the heating contribution of oxidation related cathode reactions are

$$\left(\frac{dT}{dt}\right)_{Cat,i} = \begin{cases} 0, & t - \tau_{O2} < \tau_{ign} \\ \Delta h_{Cat,i}\frac{d\alpha_i}{dt}, & t - \tau_{O2} \geq \tau_{ign} \end{cases} \tag{24}$$

In order to see the effect of using the ignition time, the multiple literature kinetics are solved with and without using the ignition time model and, labeled "Model LitKin IT" and "Model LitKin DB" respectively.

As comparison, the first order Arrhenius kinetics are also used. The equations are given as

$$\frac{dY}{dt} = -AY exp\left(-\frac{E}{RT}\right) \tag{25}$$

$$\dot{Q}'''_{rxn} = -\rho\Delta h_R \frac{dY}{dt} \tag{26}$$

The selection of parameters is discussed in Sect. 3. This case is called as "Model 1 step" in results.

4.3. Cell Array Thermal Propagation Results

In this section, the results of 1D Finite Difference array test are presented in comparison with the experimental results. A Dirichlet boundary condition has been applied to the heating side of the array. The experimental temperature has been applied until the runaway of first cell, after runaway, the boundary condition is switched to heat loss condition to the insulation block. Since preheating and triggering part is not in the scope of this paper, the results are presented starting from the second cell. 100 finite different nodes are used for each cell and 60 finite different nodes are used for each insulation block, which corresponds to a total nodes of 1240. Time step is selected as 0.001 s. Please note that the solution of the reactions are integrated by using RK45 within each time step, which uses smaller step size to achieve an absolute tolerance of 10^{-8} for the progress variable and 10^{-3} for the temperature. The computation time for the 300 s simulation was 380 s.

In the experiment, the batteries releases hot gases in the pressure vessel, the unburned batteries are heated by convection. The convection coefficient is taken as $h = 5$ W/m^{2}K. The experimental data is used for ambient temperature, which varies over time. It was observed that the latest cells were preheated up to 40°C before the runaway event, which caused a faster propagation rate near the end. Since the convection coefficient may vary over time due to venting, a constant heating rate of 0.091°C/s is applied to the cells after the runaway starts for the 1st cell to test the capability of kinetic parameters to catch the speed-up in propagation due to preheating.

In Fig. 7, the time histories of the battery surface temperatures are presented. The model predictions are in a good agreement with the experimental results. The maximum temperatures are underpredicted by the model, which may have multiple reasons. In the experiment, the ignited cell (which is not presented here) reached a higher temperature than the other cells, which may provide additional heating to the other cells, even after the reaction has ended. Additionally, the total heat of reactions may be underestimated in the model. Since the literature data varied, especially for cathode related combustion reactions, a high uncertainty is expected for the heat of reaction. The propagation time for the last cell was overpredicted. The reason can be the insulation at the end of the stack. Inaccuracies in predicting the heat losses at the end of the stack will lead to errors in the propagation time.

When the cell surface temperatures are tracked on the cell surfaces, humps are observed at different temperatures. Many researchers have observed humps at around 450°C in previous propagation studies. [2, 3, 5] They explained that these humps exist due to the time required to transfer suffcent heat through the cell packages to trigger the adjacent cell into thermal runaway. Although, pouch packaging material might also introduce a certain heat capacity and contact resistance, since the cell stack is initially under a compressive stress and the pouch packaging is thin aluminum (0.1 mm), this effect may be small. Thus, the effects of contact resistance have not been considered in the model. We believe that the observed humps represent the a thermal switch triggering specific reactions in the cell.
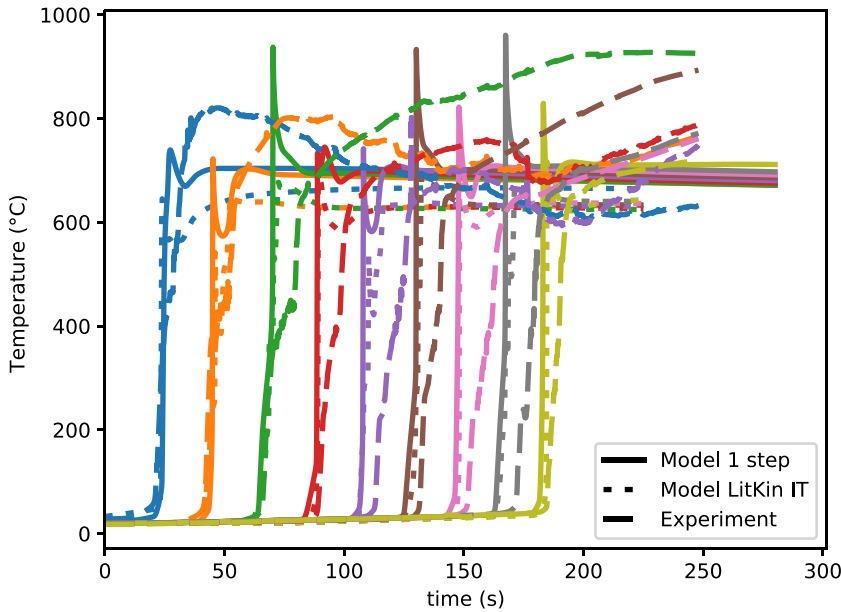
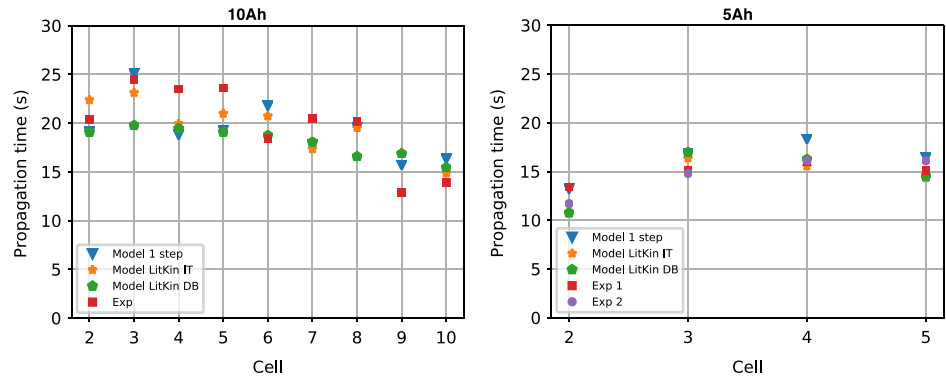**Fig. 7.** **The time history of surface temperatures of the cells (10 × 10 Ah case).**

Fig. 8. **Propagation time of cells (Left: 10 Ah; Right: 5 Ah).**

In Fig. 8, propagation times, which are the time differences between thermal runaway onset in adjacent cells, are presented for both 10 Ah and 5 Ah tests. In the experiments, the propagation times are predicted to be around 24 s for 10 Ah cells and 16 s for 5 Ah cells, which correspond to a propagation speed (using a characteristic cell length) of 0.42 mm/s and 0.55 mm/s respectively. Model predictions are very close to experimental results. The model that uses the literature kinetics with an ignition time predicted the propagation speed as 0.47mm/s and 0.55 mm/s for 10Ah and 5Ah cells respectively. The speed-up in 5 Ah cells may be

explained by the energy densities of these batteries. If we define energy density as the electrical energy per battery mass, 5 Ah cell have 15% more energy density than 10 Ah cell since it is a more compact design.

In the model, the propagation time is calculated by using the progress variable of the first stage reaction. Experimentally, the difference between the runaway start times are considered. For both 10 Ah and 5Ah cases, all model predictions are in a good agreement with the experimental result. The one step reaction was determined to fit the propagation time for 10 Ah cell, which was also accurate to predict the other cells. During the simulation, this one step kinetics was able to initiate runaway after 400°C, which means the low temperature kinetics could not be represented well. Although the heat of reactions are low for anode reactions which occurs between 200°C and 400°C range, they trigger the runaway cascade and are important to predict the propagation time.

In Fig. 9, the average mass fluxes of the cells are presented. The average mass flux is calculated by using the average propagation speed, which is defined as the battery thickness over propagation time as

$$S = \frac{\delta \bar{\dot{\omega}}_F''' A_c L_{bat}}{m_{bat}} = \frac{\dot{m}'' A_c L_{bat}}{m_{bat}} \approx \frac{L_{bat}}{\tau_{prop}} \tag{27}$$

Using the average propagation speed, the mass flux can be calculated as

$$\dot{m}'' = \rho_u S \tag{28}$$

The mass fluxes are around 1 kg/m²s and 1.5 kg/m²s for 10 Ah and 5 Ah cells respectively. As discussed earlier, there was preheating of unburned cells over time after the runaway of the due to the hot gases in the environment that had been released by the previously reacted cells. The speed-up at the end of the array could be captured with preheating only, which means the convective heating of cells by exterior hot combustion gases plays an important role in propagation
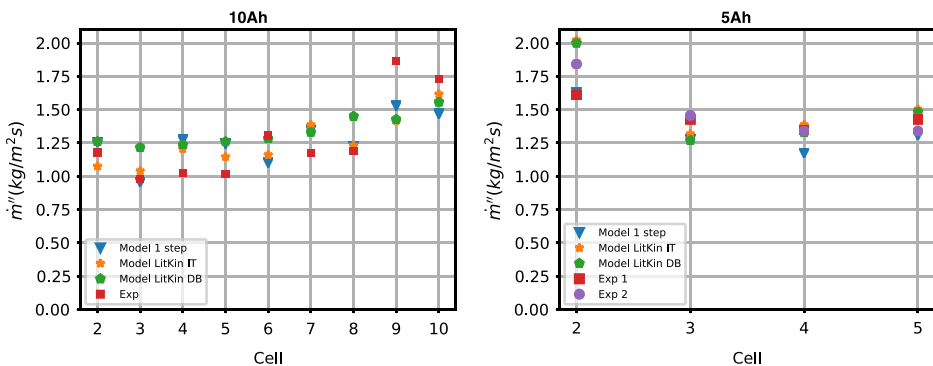

Fig. 9. Mass fluxes of cells (Left: 10 Ah; Right: 5 Ah).

times. There are deviations in the predictions that may be due to uncertainties of the thermophysical or kinetic parameters used in the model. Moreover, cold boundaries are difficult to handle in flame/reaction propagation problems such as this.

5. Conclusions

In this paper, the thermal runaway propagation through a pouch cell stack has been examined. The heat transfer through the cell stack is solved with a 1D finite difference approach. First, a comprehensive literature survey has been done for various thermal runaway reactions that may occur in the cell. The available models were evaluated and discussed. There are inconsistencies and lack of information in the literature, especially for cathode reactions and behaviour of the reaction kinetics when combined and solved at elevated temperatures. It was found that the cathode decomposition was critical, but the clear characterization of LCO decomposition and its associated combustion mechanisms are missing. These reactions are usually characterized by using slow heating tests, however they may occur differently in fast heating cases. In application of multiple thermal runaway reactions in the 1D finite difference model, the onset temperature of the cathode reactions (associated with combustion) is determined by the ignition time analysis (see "Appendix"). Although the combustion onset temperature is delayed, it did not have a significant effect on the propagation speed. Using the insights gained from the literature, a global first order Arrhenius type reaction is characterized by using the laminar premixed flame propagation theory. Using a combination of multiple thermal reactions and the global one step reaction in the 1D finite difference model, the thermal runaway propagation speed could be succesfully predicted for both 5 Ah and 10 Ah cell arrays. As propagating thermal runaway occurs, a speed up is observed in the overall rate. This speed-up is associated with a preheating of unburned cells over time due to hot combustion products available in the pressure vessel, which could be captured by the models. Uncertainties in reaction and diffusion parameters of the battery and the contact resistance between batteries might affect the propagation time predictions, which need to be further investigated. Also, investigation of compartmentalization effects on the propagation speed is necessary, which may be the case in a real module.

Acknowledgements

Appendix: Ignition Time Discussion

There are various hydrocarbons that may present when oxygen is available in the cell. The main fuel source is the electrolyte. Since DMC and DEC have high vapor pressures at low temperatures (low boiling tempearture), a significant amount of them might be vented before the presence of oxygen. Therefore, we assumed that when oxygen appears at around 240°C, the available fuel is rich for EC and its related Lithium-Electrolyte reaction (labeled as A3 or AnE in the text) product, ethylene (C_2H_4). Varatharajan and Williams [33] examined the ignition and detonation characteristics of ethylene extensively. At low temperatures, the ignition consist of a chain-branching stage and a constant concentration stage. In the chain-branching stage, the ethylene and oxygen starts forming radicals such as HO_2 and H_2O_2. In the study [33], it is shown that the time of this chain-branching stage can be determined by the concentration of the HO_2 radical. Thus, a reduced order chemical model is applied for the chain-branching stage and the time evolution for HO_2 concentration has been modeled. [33] The evolution of the radical HO_2 is given as

$$\frac{d[HO_2]}{dt} = [4 - q - s(2 - q)]\alpha_{16}[C_2H_4] + [7 - 6s - 3q(1 - s)]\alpha_{20}[HO_2] \\ - k_{10}[HO_2]^2 \tag{29}$$

Chain-branching stage will end when the concentration of HO_2 will reach the following

$$[HO_2] = \frac{[7 - 6s - 3q(1 - s)]\alpha_{20}}{k_{10}} \tag{30}$$

k and α are the reaction rates such as

$$k_i = A_i T^{n_i} \exp\left(-\frac{E_i}{RT}\right) \tag{31}$$

$$\alpha_{16} = k_{16}[O_2] \tag{32}$$

$$\alpha_{20} = k_{20}[C_2H_4] \tag{33}$$

q and s are also related with reaction rates such as

$$q = \frac{\alpha_{18}}{\alpha_{18} + \alpha_{19}} \tag{34}$$

$$s = \frac{\alpha_{25}}{\alpha_{25} + \alpha_{26}} \tag{35}$$

where the subscript numbers are associated with the number of reactions defined in Varatharajan and Williams [33]. This means, for any initial C_2H_4, O_2 concentration and temperature, the ignition time can be estimated as follows: starting with zero HO_2 concentration, Eq. 29 can be integrated, and the ignition happens when HO_2 concentration reaches the value determined by Eq. 30. This is often called numerical estimation. Varatharajan and Williams [33] also developed an analytical formula to estimate the chain-branching time as

$$\tau_{cb} = \frac{1}{[7 - 6s - 3q(1-s)]\alpha_{20}} \ln\left(1 + \frac{\alpha_{20}^2[7 - 6s - 3q(1-s)]^2}{\alpha_{16}[C_2H_4]k_{10}[4 - q - s(2-q)]}\right) \quad (36)$$

Therefore, the ignition time can either be evaluated by using the analytical formula in Eq. 36, or numerically. Further details can be found in Varatharajan and Williams [33].

Concisely, the ignition time can be written as a function of temperature and initial fuel and oxygen concentrations as

$$\tau_{ign} = f(T, C_{C_2H_4}, C_{O_2}) \quad (37)$$

Fuel and oxygen concentrations are determined by using a mixture concentration and an equivalence ratio. Using the equation of state, the concentration of the mixture can be evaulated as

$$C_{mix} = \frac{P}{RT} \quad (38)$$

In Eq. 38, P is the total pressure of the gas mixture and R is the specific gas constant. The concentration of the mixture can be distributed to the fuel and oxygen based on the equivalence ratio (ϕ) as follows

$$C_{C_2H_4} = C_{mix}\frac{\phi}{3 + \phi} \quad (39)$$

$$C_{O_2} = C_{mix}\frac{3}{3 + \phi} \quad (40)$$

Since the experiment was performed in a nitrogen environment, the oxygen that caused combustion must be provided by LCO decomposition. Many researchers observed the oxygen after 240°C or associated exothermic reactions to oxidation of electrolyte after 200°C. At this temperature, there can be flammable hydrocarbons in the cell due to Anode–Electrolyte reaction or electrolyte evaporation. As long as there is oxygen and fuel in the cell, combustion might occur, providing a sufficient time for auto-ignition. At low temperatures, the ignition times can be high due to long chain branching stages. For stoichiometric ethylene–oxygen
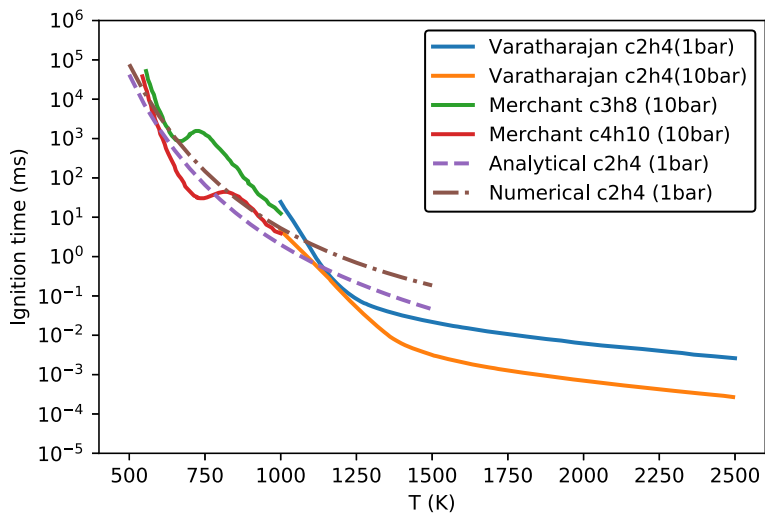
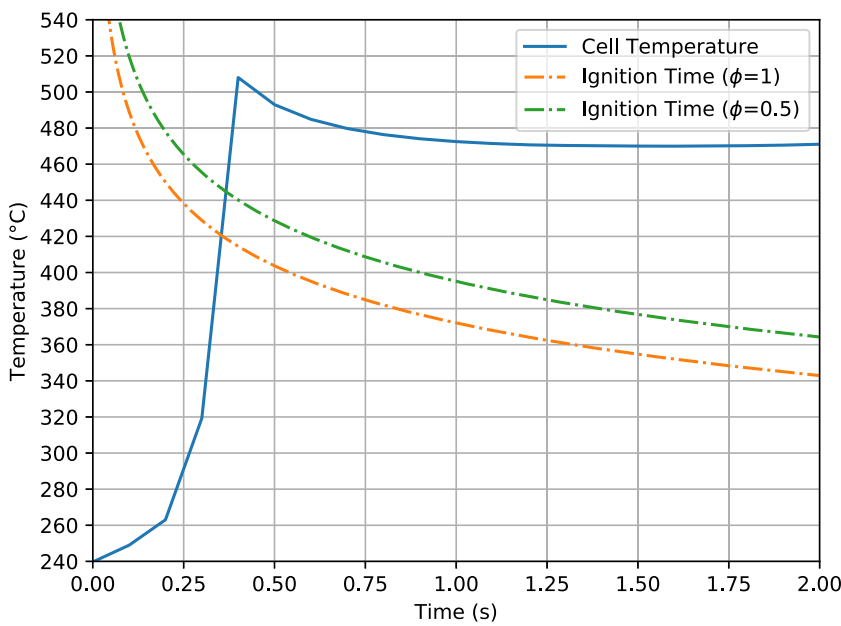**Fig. 10.** Ignition time prediction for stoichiometric ethylene–oxygen mixture at 1 bar.

Fig. 11. Time history of the battery temperature after runaway in comparison with the ignition time prediction.

mixture at 1 bar, the ignition times are predicted using the aforementioned analytical and numerical models and compared with the values in the literature in Fig. 10. The data provided by Varatharajan are evaluated by using detailed chemical mechanisms. Please note that for temperatures lower than 1000 K, Varatharajan does not provide ignition time data. Therefore, as a sanity check, we presented the ignition times of propane and butane in this low temperature (500 K to 1000 K) range [34]. The results are in a reasonable agreement.

At the lower temperatures for which the oxygen–hydrocarbon mixture may present in the cell, (after 240°C), assuming that the oxygen starts to be present after 240°C, it is possible to estimate the onset temperature of thermal runaway by evaluating the ignition time after oxygen is generated. Ignition is assumed to happen when the ignition time is achieved

$$t_{runaway} = t_{240°C} + \tau_{ign} \tag{41}$$

A representative temperature profile is compared with the ignition times that are evaluated by the numerical model in Fig. 11. At the left-hand side of the dashed dot and solid curve intersection, the cell temperature is low and corresponding required ignition time is so high that the necessary conditions for ignition could not be achieved. When temperature is increased and intersected with the ignition time prediction, a sufficient time has been passed after the presence of oxygen and fuel, which makes the ignition possible. For the ignition time prediction, the pressure is set to 1.2 bar, which is measured by the load cell in the experiment.

References

1. Lopez CF, Jeevarajan JA, Mukherjee PP (2015) Experimental analysis of thermal runaway and propagation in lithium-ion battery modules. J Electrochem Soc 162(9):A1905–A1915. https://doi.org/10.1149/2.0921509jes
2. Feng X et al (2015) Characterization of penetration induced thermal runaway propagation process within a large format lithium ion battery module. J Power Sources 275:261–273. https://doi.org/10.1016/j.jpowsour.2014.11.017
3. Feng X, Lu L, Ouyang M, Li J, He X (2016) A 3D thermal runaway propagation model for a large format lithium ion battery module. Energy 115:194–208. https://doi.org/10.1016/j.energy.2016.08.094
4. Qi C, Zhu Y, Gao F, Yang K, Jiao Q (2018) Mathematical model for thermal behavior of lithium ion battery pack under overcharge. Int J Heat Mass Transf 124:552–563. https://doi.org/10.1016/j.ijheatmasstransfer.2018.03.100
5. Gao S et al (2019) Experimental study on module-to-module thermal runaway-propagation in a battery pack. J Electrochem Soc 166(10):A2065–A2073. https://doi.org/10.1149/2.1011910jes
6. Said AO, Lee C, Stoliarov SI, Marshall AW (2019) Comprehensive analysis of dynamics and hazards associated with cascading failure in 18650 lithium ion cell arrays. Appl Energy 248:415–428. https://doi.org/10.1016/j.apenergy.2019.04.141
7. Wang Q, Ping P, Zhao X, Chu G, Sun J, Chen C (2012) Thermal runaway caused fire and explosion of lithium ion battery. J Power Sources 208:210–224. https://doi.org/10.1016/j.jpowsour.2012.02.038

8. Feng X, Ouyang M, Liu X, Lu L, Xia Y, He X (2018) Thermal runaway mechanism of lithium ion battery for electric vehicles: a review. Energy Storage Mater 10:246–267. https://doi.org/10.1016/j.ensm.2017.05.013

9. Richard MN, Dahn JR (1999) Accelerating rate calorimetry study on the thermal stability of lithium intercalated graphite in electrolyte. I. Experimental. J Electrochem Soc 146(6):2068–2077. https://doi.org/10.1149/1.1391893

10. Richard MN, Dahn JR (1999) Accelerating rate calorimetry study on the thermal stability of lithium intercalated graphite in electrolyte. II. Modeling the results and predicting differential scanning calorimeter curves. J Electrochem Soc 146(6):2078–2084. https://doi.org/10.1149/1.1391894

11. Wang Q, Sun J, Yao X, Chen C (2006) Thermal behavior of lithiated graphite with electrolyte in lithium-ion batteries. J Electrochem Soc 153(2):A329–A333. https://doi.org/10.1149/1.2139955

12. Maleki H, Deng G, Kerzhner-Haller I, Anani A, Howard JN (2000) Thermal stability studies of binder materials in anodes for lithium-ion batteries. J Electrochem Soc 147(12):4470–4475. https://doi.org/10.1149/1.1394088

13. Feng X et al (2015) Thermal runaway propagation model for designing a safer battery pack with 25 Ah LiNi Co MnO$_2$ large format lithium ion battery. Appl Energy 154:74–91. https://doi.org/10.1016/j.apenergy.2015.04.118

14. Hatchard TD, MacNeil DD, Basu A, Dahn JR (2001) Thermal model of cylindrical and prismatic lithium-ion cells. J Electrochem Soc 148(7):A755–A761. https://doi.org/10.1149/1.1377592

15. Kriston A, Adanouj I, Ruiz V, Pfrang A (2019) Quantification and simulation of thermal decomposition reactions of Li-ion battery materials by simultaneous thermal analysis coupled with gas analysis. J Power Sources 435:226774. https://doi.org/10.1016/j.jpowsour.2019.226774

16. Ren D et al (2018) Model-based thermal runaway prediction of lithium-ion batteries from kinetics analysis of cell components. Appl Energy 228:633–644. https://doi.org/10.1016/j.apenergy.2018.06.126

17. MacNeil DD, Dahn JR (2001) The reaction of charged cathodes with nonaqueous solvents and electrolytes: I. LixCoO$_2$. J Electrochem Soc 148(11):A1205. https://doi.org/10.1149/1.1407245

18. MacNeil DD, Dahn JR (2001) The reaction of charged cathodes with nonaqueous solvents and electrolytes: II. LiMn$_2$O$_4$ charged to 4.2 V. J Electrochem Soc 148(11):A1211. https://doi.org/10.1149/1.1407246

19. MacNeil DD, Dahn JR (2001) Test of reaction kinetics using both differential scanning and accelerating rate calorimetries as applied to the reaction of LixCoO$_2$ in non-aqueous electrolyte. J Phys Chem A 105(18):4430–4439. https://doi.org/10.1021/jp001187j

20. MacNeil DD, Dahn JR (2002) The reactions of Li$_{0.5}$CoO$_2$ with nonaqueous solvents at elevated temperatures. J Electrochem Soc 149(7):A912. https://doi.org/10.1149/1.1483865

21. Wang Q, Sun J, Yao X, Chen C (2005) Thermal stability of LiPF6/EC + DEC electrolyte with charged electrodes for lithium ion batteries. Thermochim Acta 437(1–2):12–16. https://doi.org/10.1016/j.tca.2005.06.010

22. Baba Y, Okada S, Yamaki J (2002) Thermal stability of LixCoO$_2$ cathode for lithium ion battery. Solid State Ion 148(3–4):311–316. https://doi.org/10.1016/S0167-2738(02)00067-X

23. Wang L, Maxisch T, Ceder G (2007) A first-principles approach to studying the thermal stability of oxide cathode materials. Chem Mater 19(3):543–552. https://doi.org/10.1021/cm620943

24. Jiang J, Dahn JR (2004) ARC studies of the thermal stability of three different cathode materials: LiCoO$_2$; Li[Ni0.1Co0.8Mn0.1]O$_2$; and LiFePO$_4$, in LiPF6 and LiBoB EC/DEC electrolytes. Electrochem Commun 6(1):39–43. https://doi.org/10.1016/j.elecom.2003.10.011

25. Yamaki J, Shinjo Y, Doi T, Okada S (2014) The rate equation for oxygen evolution by decomposition of Li$_x$CoO$_2$ at elevated temperatures. J Electrochem Soc 161(10):A1648–A1654. https://doi.org/10.1149/2.0621410jes

26. Furushima Y, Yanagisawa C, Nakagawa T, Aoki Y, Muraki N (2011) Thermal stability and kinetics of delithiated LiCoO$_2$. J Power Sources 196(4):2260–2263. https://doi.org/10.1016/j.jpowsour.2010.09.076

27. Jung D-H, Umirov N, Kim T, Bakenov Z, Kim J-S, Kim S-S (2019) Thermal and structural stabilities of LixCoO$_2$ cathode for Li secondary battery studied by a temperature programmed reduction. Eurasian Chem-Technol J 1:3. https://doi.org/10.18321/ectj780

28. Ping P, Wang Q, Huang P, Sun J, Chen C (2014) Thermal behaviour analysis of lithium-ion battery at elevated temperature using deconvolution method. Appl Energy 129:261–273. https://doi.org/10.1016/j.apenergy.2014.04.092

29. Wang QS, Sun JH, Chen CH, Zhou XM (2008) Thermal properties and kinetics study of charged LiCoO$_2$ by TG and C80 methods. J Therm Anal Calorim 92(2):563–566. https://doi.org/10.1007/s10973-007-8289-z

30. Law CK (2010) Combustion physics. Cambridge University Press, Cambridge

31. Bilyaz S, Archibald E, Marr KC, Ezekoye OA (2019) Parameter estimation for battery kinetic and thermophysical parameters. In: ASTFE Digital Library

32. Somandepalli V, Marr K, Horn Q (2014) Quantification of combustion hazards of thermal runaway failures in lithium-ion batteries. SAE Int J Altern Powertrains 3:98–104. https://doi.org/10.4271/2014-01-1857

33. Varatharajan B, Williams FA (2002) Ethylene ignition and detonation chemistry, part 2: ignition histories and reduced mechanisms. J Propuls Power 18(2):352–362. https://doi.org/10.2514/2.5941

34. Merchant SS, Goldsmith CF, Vandeputte AG, Burke MP, Klippenstein SJ, Green WH (2015) Understanding low-temperature first-stage ignition delay: propane. Combust Flame 162(10):3658–3673. https://doi.org/10.1016/j.combustflame.2015.07.005